1-1-2020

A Long Cycle-Life High-Voltage Spinel Lithium-Ion Battery Electrode Achieved by Site-Selective Doping

Gemeng Liang
University of Wollongong, gl906@uowmail.edu.au

Zhibin Wu
University of Wollongong, zw120@uowmail.edu.au

Christophe R. Didier
University of Wollongong, cdidier@uow.edu.au

Wenchao Zhang
University of Wollongong, wenchao@uow.edu.au

Jing Cuan
University of Wollongong

See next page for additional authors

A Long Cycle-Life High-Voltage Spinel Lithium-Ion Battery Electrode Achieved by Site-Selective Doping

Abstract

© 2020 Wiley-VCH Verlag GmbH & Co. KGaA, Weinheim Spinel LiNi0.5Mn1.5O4 (LNMO) is a promising cathode candidate for the next-generation high energy-density lithium-ion batteries (LIBs). Unfortunately, the application of LNMO is hindered by its poor cycle stability. Now, site-selectively doped LNMO electrode is prepared with exceptional durability. In this work, Mg is selectively doped onto both tetrahedral (8a) and octahedral (16c) sites in the Fd (Formula presented.) m structure. This site-selective doping not only suppresses unfavorable two-phase reactions and stabilizes the LNMO structure against structural deformation, but also mitigates the dissolution of Mn during cycling. Mg-doped LNMOs exhibit extraordinarily stable electrochemical performance in both half-cells and prototype full-batteries with novel TiNb2O7 counter-electrodes. This work pioneers an atomic-doping engineering strategy for electrode materials that could be extended to other energy materials to create high-performance devices.

Disciplines

Engineering | Physical Sciences and Mathematics

Publication Details

Liang, G., Wu, Z., Didier, C., Zhang, W., Cuan, J., Li, B., Ko, K., Hung, P., Lu, C., Chen, Y., Leniec, G., Kaczmarek, S., Johannessen, B., Thomsen, L., Peterson, V., Pang, W. & Guo, Z. (2020). A Long Cycle-Life High-Voltage Spinel Lithium-Ion Battery Electrode Achieved by Site-Selective Doping. Angewandte Chemie - International Edition,

Authors

Gemeng Liang, Zhibin Wu, Christophe R. Didier, Wenchao Zhang, Jing Cuan, Baohua Li, Kuan-Yu Ko, Po Hung, Cheng Lu, Yuanzhen Chen, Grzegorz Leniec, Slawomir Kaczmarek, Bernt Johannessen, Lars Thomsen, Vanessa K. Peterson, Wei Kong Pang, and Zaiping Guo

RESEARCH ARTICLE

A long cycle-life high-voltage spinel lithium-ion battery electrode achieved by site-selective doping

Gemeng Liang[a], Zhibin Wu[a], Christophe Didier[a, b], Wenchao Zhang[a], Jing Cuan[a], Baohua Li[c], Kuan-Yu Ko[d], Po-Yang Hung[d], Cheng-Zhang Lu[d], Yuanzhen Chen[e], Grzegorz Leniec[f], Sławomir Maksymilian Kaczmarek[f], Bernt Johannessen[g], Lars Thomsen[g], Vanessa K. Peterson[a, b], Wei Kong Pang*[a], and Zaiping Guo*[a]

Abstract: Spinel $LiNi_{0.5}Mn_{1.5}O_4$ (LNMO) is a promising cathode candidate for the next-generation high energy-density lithium-ion batteries (LIBs). Unfortunately, the application of LNMO is hindered by its poor cycle stability. Here, we demonstrate an easily-prepared site-selectively doped LNMO electrode with exceptional durability. In this work, Mg is selectively doped onto both tetrahedral (8*a*) and octahedral (16*c*) sites in the $Fd\bar{3}m$ structure. This site-selective doping not only suppresses unfavorable two-phase reactions and stabilizes the LNMO structure against structural deformation, but also mitigates the dissolution of Mn during cycling. Mg-doped LNMOs exhibit excellent electrochemical performance, retaining ~ 86% and ~ 87% of initial capacity after 1500 cycles at 1 C and 2200 cycles at 10 C, respectively. Such excellent electrochemical performance is also reflected in prototype full-batteries with novel $TiNb_2O_7$ counter electrodes. This work pioneers an atomic-doping engineering strategy for electrode materials that could be extended to other energy materials to create high-performance devices.

Introduction

Lithium-ion batteries (LIBs) form an important part of our daily life, powering portable electronic devices, as well as electric and hybrid electric vehicles, due to their long-service life, high energy density, and reasonably low environmental impact.[1] Considering the significant technological revolution brought about by LIBs, the 2019 Nobel Prize in Chemistry was awarded to John B. Goodenough, M. Stanley Whittingham, and Akira Yoshino for their invaluable contribution to the development of LIBs. However, further enhancement is still needed to meet the increasing requirements of rapidly developing technologies. Intense effort is focused on the development of electrode materials for LIBs with high specific capacity and energy density.[1c] Spinel $LiNi_{0.5}Mn_{1.5}O_4$ (LNMO) is considered one of the most promising electrode candidates for next-generation high energy-density LIBs due to its high operating voltage of 4.7 V vs. Li/Li^+, high energy density approaching 650 Wh kg^{-1}, low fabrication cost, and fast lithium diffusion.[2] Unfortunately, LNMO suffers from rapid capacity decay and unsatisfactory cycle stability, limiting its practical application and commercialization.[2b, 3] To enhance the electrochemical stability of LNMO, various doping strategies have been widely adopted.[4] Although the electrochemical performance of LNMO is enhanced through doping, the mechanism by which the performance is improved remains unclear, with the chemistry- and structure-function relations for chemically-modified LNMOs relatively unknown.

Lin *et al.* explored the atomic structure evolution of functioning LNMO by aberration-corrected scanning transmission electron microscopy (STEM).[5] Interestingly, Mn_3O_4-like spinel and rock-salt structures were found to form on the surface and subsurface of LNMO particles, due to the migration of transition metals (TM) into tetrahedral (8*a* sites of $Fd\bar{3}m$) and octahedral sites (16*c* sites of $Fd\bar{3}m$), respectively. These irreversible phase transformations initiated through TM migration lead to the TM dissolution and increased charge transfer impedance, severely deteriorating battery performance. Xiao *et al.* used atomic layer deposition (ALD) coupled with post-treatment to incorporate Ti^{4+} into surface $Fd\bar{3}m$ 8*a* sites,[6] with this relieving impedance accumulation and alleviating side reactions at the electrode-electrolyte interphase. Piao *et al.* doped Al^{3+} into empty $Fd\bar{3}m$ 16*c* octahedral sites at LNMO surface by ALD and heat treatment,[7] suppressing TM dissolution and reducing side reactions with the electrolyte. Therefore, doping at both tetrahedral and octahedral sites is evidently the key to the structural stabilization of LNMO during long-term cycling. Moreover, a facile and low-cost atomic-doping-engineering strategy to effectively improve LNMO performance is also urgently needed.

Herein, we proposed a strategy to dope Mg into LNMO that site-selectively targets both 8*a* and 16*c* crystallographic sites within the $Fd\bar{3}m$ structure through a facile solid-state-reaction. The similar ionic radii of Mg ions at both tetrahedral and octahedral sites in LNMO (0.57 and 0.72 Å, respectively) avoids significant

[a] G. Liang, Z. Wu, Dr. C. Didier, Dr. W. Zhang, Dr. J.Cuan, Dr. W. K. Pang, Prof. Z. Guo
Faculty of Engineering, Institute for Superconducting & Electronic Materials, University of Wollongong, Wollongong, NSW, Australia
E-mail: wkpang@uow.edu.au (W. K. Pang); zguo@uow.edu.au (Z. Guo)
[b] Dr. C. Didier, Dr. V. K. Peterson
Australian Centre for Neutron Scattering, Australian Nuclear Science and Technology Organization, Sydney, NSW, Australia
[c] Prof. B. Li
Graduate School at Shenzhen, Tsinghua University, Shenzhen 518055, PR China
[d] K. Ko, P. Hung, Dr. C. Lu
Industrial Technology Research Institute, Hsinchu, Taiwan, China
[e] Dr. Y. Chen
School of Materials Science and Engineering, Xi'an Jiaotong University, Xi'an 710049, PR China
[f] Dr. G. Leniec, Dr. S. M. Kaczmarek
Faculty of Mechanical Engineering and Mechatronics, West Pomeranian University of Technology in Szczecin, Al. Piastów, 17, 70-310 Szczecin, Poland
[g] Dr. B. Johannessen, Dr. L. Thomsen
Australian Synchrotron, Australian Nuclear Science and Technology Organization, 800 Blackburn Road, Clayton, Victoria, 3168, Australia

Supporting information for this article is given via a link at the end of the document.

structural distortion.[8] This work extends on previous work reporting electrochemical properties of Mg-doped LNMO,[4b, 4c, 9] revealing the effects of Mg doping on the LNMO structure using a range of crystallographic, local structure, as well as morphological characterization tools. We report in detail the chemistry- and structure-function relations of Mg-doped LNMO for the first time, applying electrochemical testing alongside in operando synchrotron-based X-ray powder diffraction (XRPD) and neutron powder diffraction (NPD) to confirm the role of the Mg dopant in suppressing Mn dissolution, stabilization of the spinel structure, and modifying LNMO phase transformations during cycling. Further, the excellent performance of the Mg-doped LNMO electrode is coupled with a $TiNb_2O_7$ (TNO) electrode in a full-cell configuration, verifying further the success of our site-selective doping strategy. Importantly, as Mg^{2+} can occupy tetrahedral or octahedral sites in a variety of structures such as octahedral sites in MgO and tetrahedral sites in $MgAl_2O_4$, this doping strategy can be easily extended to other electrode materials to enhance battery electrochemical performance and extend cell service life. Finally, the high natural abundance of Mg in the Earth's crust makes it low cost as a promising dopant.[10]

Results and Discussion

Morphology and crystal structure characterization

Scanning electron microscopy (SEM) images of LNMO and LNMO doped with different Mg concentrations are displayed in **Figure S1**, showing that the addition of Mg dopants doesn't substantially influence the shape or size of the particles. $LiNi_{0.5}Mn_{1.5}O_4$, $LiMg_{0.05}Ni_{0.5}Mn_{1.5}O_4$, $LiMg_{0.1}Ni_{0.5}Mn_{1.5}O_4$, and $LiMg_{0.15}Ni_{0.5}Mn_{1.5}O_4$ are abbreviated to LNMO, Mg0.05-LNMO, Mg0.1-LNMO, and Mg0.15-LNMO, respectively, in the following discussion. **Figure 1a and 1b** show SEM and transmission electron microscopy (TEM) micrographs, respectively, of Mg0.1-LNMO sample, noting that the truncated-octahedron morphology is similar to LNMO previously reported.[11] Energy dispersive spectroscopy (EDS) results (**Figure 1c**) confirm the uniform distribution of Ni, Mn, Mg, and O in the Mg0.1-LNMO sample. **Figure 1d** shows in detail the selected area in **Figure 1b**. Two different facets of the truncated octahedron are revealed in high-resolution TEM images, corresponding to the (222) plane with a lattice spacing of ~ 0.23 nm (**Figure 1e**)[12] and the (400) plane with an interplanar distance of ~ 0.20 nm (**Figure 1f**)[11a] of the highly crystalline *Fd*$\bar{3}$*m* structure.

To verify our site-selective doping and better understand the structural differences induced by Mg doping, STEM was employed in high-angle annular dark-field (HAADF) mode, enabling direct observation of the atomic-level crystal structure. The STEM HAADF images of LNMO and Mg0.1-LNMO (**Figure 1g and 1h**, respectively) are viewed along the [110] direction, allowing identification of the positions of the heavy atomic columns.[5, 7] We note that the observed bright atomic columns in the images correspond to heavy atoms, whilst lighter elements such as Li and O are undetectable. In LNMO (**Figure 1g and 1i**), a typical diamond-shape atomic structure is observed, confirming its spinel structure as consistent with previous STEM observations.[5, 7] Line-profile analysis (**Figure 1j**) shows continuous peaks with an interval of approximately 0.8 nm in the LNMO structure, coinciding well with the diagonal distance of two TM atoms within the spinel structure.[5] When the Mg dopant is introduced, the spinel framework persists, as shown in **Figure 1h**. **Figure 1k** shows in detail the selected region (yellow box) in **Figure 1h**, where two new diamond-like frameworks are clearly observed. One is the center-filled diamond where Mg occupies the previously-empty 16*c* octahedral site, and the other is a diamond containing two atoms corresponding to the occupation of the tetrahedral site (8*a*) by Mg, indicating that Mg partially replaces Li at the 8*a* sites. The corresponding line profiles are shown in **Figure 1l and 1m**. Taken together, these characterizations confirm the successful doping of Mg at both 16*c* and 8*a* sites in the LNMO structure.

X-ray photoelectron spectroscopy (XPS) provides further evidence of the successful site-selective doping. **Figure 2a** shows the Mg 2*p* spectra of MgO, $MgAl_2O_4$, Mg0.05-LNMO, and Mg0.1-LNMO. Mg^{2+} is known to locate at octahedral and tetrahedral sites within MgO and $MgAl_2O_4$, respectively, reflected by the peak positions (i.e. binding energy) of ~ 49.6 eV and ~ 52.7 eV, respectively, in Mg 2*p* spectra.[13] The spectra of Mg-doped LNMO are split into these peaks, further confirming the STEM results. Interestingly, the ratio between tetrahedral and octahedral doping in LNMO is found to change, where increases in Mg content result in the increased occupation of Mg at the tetrahedral site. Soft X-ray (SXR) results (**Figure 2b**) also support the success of this two-site-doping strategy, where the white line and inflection point energies of Mg0.1-LNMO are similar to those of MgO, revealing the existing octahedral-site Mg, meanwhile, the emerging pre-edge (dashed box) in Mg0.1-LNMO, corresponding to the 1*s*-3*d* quadrupole transition, indicates Mg in a tetrahedral environment.[14]

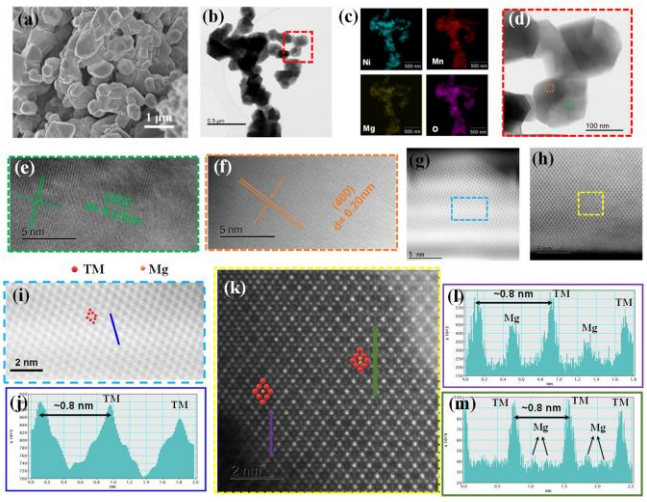

Figure 1. (a) SEM and (b) TEM images of Mg0.1-LNMO; (c) Elemental mapping for Ni, Mn, Mg and O within the Mg0.1-LNMO particles; (d) enlargement of the selected zone in (b); (e) and (f) high-resolution TEM images corresponding to the two regions in (d); typical STEM HAADF images of (g) LNMO and (h) Mg0.1-LNMO; (i) enlarged region of the light blue box in panel (g) ; (j) line profile corresponding to blue lines in panel (i); (k) enlargement of the yellow box region in panel (h); (l) and (m) line profiles corresponding to purple and olive lines in panel (k), respectively.

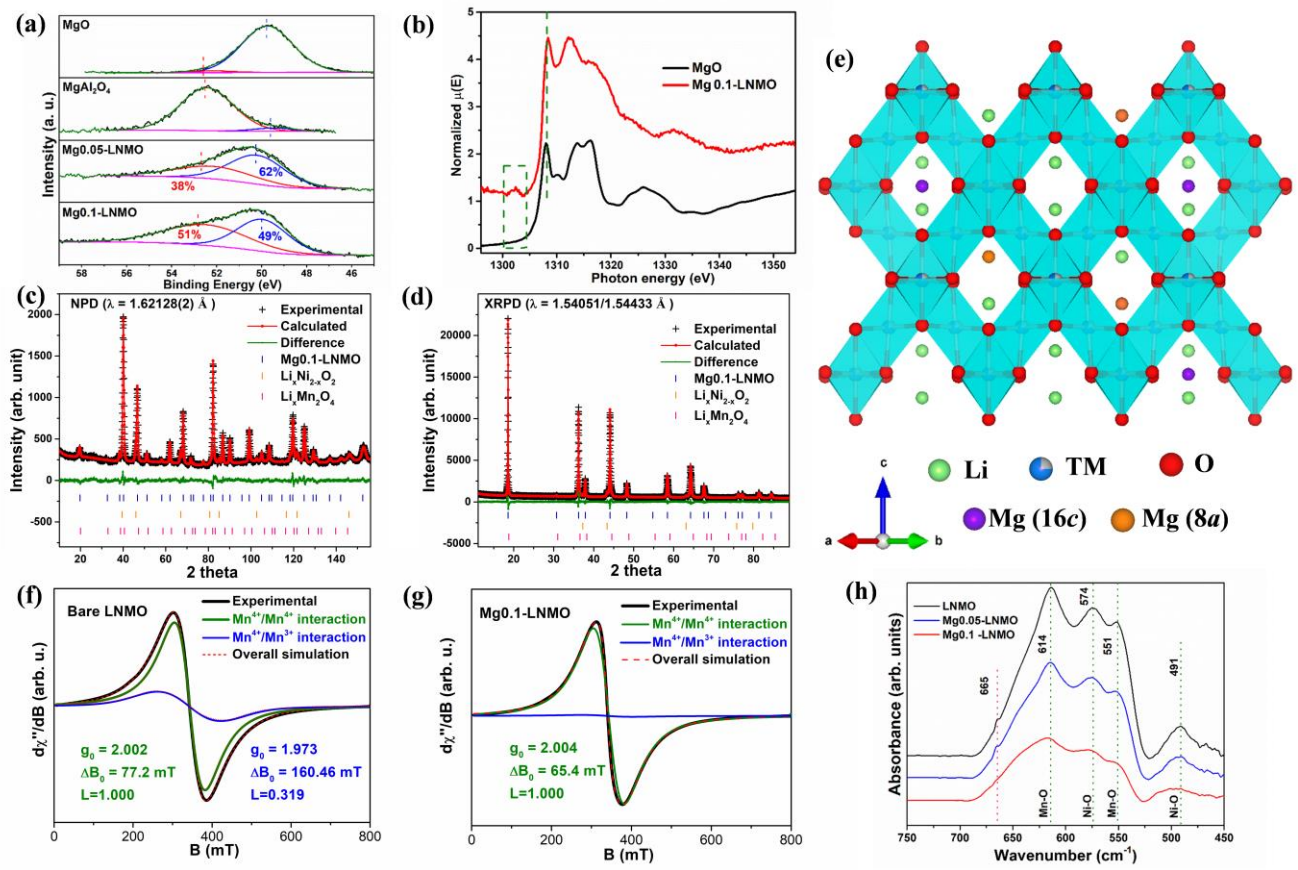

Figure 2. (a) Mg 2*p* XPS spectra of MgO, $MgAl_2O_4$, Mg0.05-LNMO and Mg0.1-LNMO samples; (b) SXR spectra of MgO and Mg0.1-LNMO; joint Rietveld refinement profiles using (c) NPD and (d) XRPD data of Mg0.1-LNMO (R_{wp} = 5.47%, combined GOF = 1.78); (e) schematic crystallographic structure of *Fd*$\bar{3}$*m* Mg0.1-LNMO; EPR spectrum and analysis of (f) LNMO and (g) Mg0.1-LNMO; (h) FT-IR spectra of LNMO, Mg0.05-LNMO, and Mg0.1-LNMO samples.

Structural investigations of LNMO and Mg0.1-LNMO were carried out by employing joint Rietveld refinement using NPD and XRPD data. The refinement results for LNMO and Mg0.1-LNMO materials are summarized in **Table S1** and refinement profiles of LNMO are displayed in **Figure S2** and of Mg0.1-LNMO in **Figure 2c and 2d**. $Li_xNi_{2-x}O_2$ (ICSD# 41890, 2.6(1) wt.%)[15] was found in the LNMO sample and the Mg0.1-LNMO sample was found to include impurities of both $Li_xNi_{2-x}O_2$ and $Li_xMn_2O_4$ phases (ICSD#50415)[16] with weight fractions of 3.4(1)% and 2.2(3)%, respectively. Although these undesirable impurities are expected to affect battery performance to some extent, they are ignored in the following discussions due to their relatively minor content.

With the aid of excellent contrast between the neutron coherent scattering length of Li (-1.90 fm) and Mg (5.375 fm), NPD clearly detects the Mg existence at the tetrahedral site (8*a*) in Mg0.1-LNMO, and determines it to be 0.7(3)% occupation. Meanwhile, the site occupation factor of Mg at *16c* site is confirmed to be 0.3(2)% in the structure. A schematic crystallographic structure of Mg0.1-LNMO is shown in **Figure 2e**, where Li and O occupy the 8*a* and 32*e* crystallographic sites, respectively, and Ni and Mn share the octahedral 16*d* sites in the *Fd*$\bar{3}$*m* structure. Mg ions were successfully introduced at both tetrahedral (8*a*) and octahedral (16*c*) sites. Furthermore, the similar lattice parameter and cell volume of the bare LNMO (*a* = 8.1774(1) Å and V = 546.83(2) $Å^3$) and Mg0.1-LNMO (*a* = *8*.1762(1) Å and V = 546.60(2) $Å^3$) samples further approve the advantage of Mg two-site doping in avoiding significant structural distortion.

Electron paramagnetic resonance (EPR) characterization was also performed on the LNMO and Mg0.1-LNMO samples (**Figure 2f and 2g**, respectively). The two EPR spectra are both characterized by a very intense and almost symmetrical EPR line at about g~2. In **Figure 2f**, the intensive green line centered at g = 2.004 with the pure Lorentz shape was attributed to ferromagnetic-like interactions of Mn^{4+}, while the weak blue line centered at g = 1.973 with Gauss-Lorentz components was assigned to ferromagnetic-like Mn^{4+}-Mn^{3+} interactions. Notably, the EPR spectrum changes significantly after Mg is introduced into LNMO (**Figure 2g**), where the spectrum narrows for Mg0.1-LNMO and becomes fully dominated by contributions from Mn^{4+}. The fully Lorentz-like shape and much smaller width of the EPR line indicate the stronger interactions between Mn^{4+} in the Mg0.1-LNMO. Moreover, the absence of Mn^{4+}-Mn^{3+} interactions in the Mg0.1-LNMO reveals a decrease in Mn^{3+} and subsequent relief of Jahn-Teller distortion as a result of Mg doping, consistent with the corresponding XPS Mn $2p_{3/2}$ spectrum (**Figure S3**).

Fourier transform infrared spectroscopy (FT-IR) is sensitive to local structures and widely employed to determine the degree of Ni/Mn ordering in spinel LNMO.[17] The intensity ratio between 614 and 574 cm^{-1} peaks allows semi-quantitative comparison of cation-ordering in LNMO, with a higher ratio corresponding to higher cation disorder.[17] Our Mg0.1-LNMO sample has the highest ratio of 1.176, followed by Mg0.05-LNMO of 1.138 and LNMO of 1.124 (**Figure 2h**), indicating that Mg increases Ni/Mn disorder in the spinel. Peaks at 665 and 551 cm^{-1} in the LNMO

spectra are characteristic peaks of ordered LNMO, and these weaken with increasing Mg content, consistent with Mg increasing cation disorder in LNMO. In addition, the thermal stability of the LNMO is also found to be improved by Mg doping (**Figure S4**).

Electrochemical performance

Figure 3a compares the cycling performance of four LNMO samples at 1 C, with Mg0.1-LNMO delivering the highest discharge specific capacity of 123.0 mAh g^{-1}, followed by Mg0.05-LNMO of 118.8 mAh g^{-1}, LNMO of 116.9 mAh g^{-1}, and Mg0.15-LNMO of 93.4 mAh g^{-1}. Moreover, the Mg0.1-LNMO sample exhibited a high discharge capacity of 106.1 mAh g^{-1} at the 1500th cycle, corresponding to a capacity retention of 86.3%, significantly higher than those for Mg0.05-LNMO and LNMO of 60.9% and 66.9%, respectively. The worst electrochemical performance was observed for the Mg0.15-LNMO sample. Obviously, the cycle stability of LNMO is found to be greatly improved by a proper amount of Mg doping at tetrahedral and octahedral sites.

The electrochemical performance of our Mg0.1-LNMO sample is significantly improved over other previously reported LNMO samples (**Figure 3b**)[4a, 6, 12b, 18]. Along with the exceptional longest-term cycling performance (1500 cycles), our Mg0.1-LNMO delivers 116.0 mAh g^{-1} and a capacity retention of 94.6% after 500 cycles, while others reported LNMOs typically maintain < 90% of their initial capacities after 500 cycles.[18c, 18h] At the 1000th cycle, our Mg0.1-LNMO retains 91.5% of initial capacity, compared with the values of less than 86% for other reported LNMOs.[4a, 18b, 18f] The enhanced cycle stability derived from the site-selective doping strategy becomes more obvious when the cycle number increases.

The corresponding charge/discharge curves of the three LNMOs (**Figure 3c)** show that the Mg0.1-LNMO sample has the smallest voltage polarization in the 100th cycle. In the 1500th cycle, the voltage polarization of the Mg0.1-LNMO sample doesn't increase substantially, while those of Mg0.05-LNMO and LNMO experience a large increase. The reduced voltage polarization of Mg0.1-LNMO is also confirmed by cyclic voltammetry (CV) scanning (**Table S2**). In addition, the smallest Mn^{3+} concentration of Mg0.1-LNMO among the three samples (**Table S3**) implies that the Mg dopant effectively stabilizes the LNMO spinel against Mn^{3+} formation during cycling.

The corresponding energy densities of the different LNMOs are shown in **Figure 3d**. Mg0.1-LNMO exhibits an energy density of 570 Wh kg^{-1} at 1 C, significantly higher than those of Mg0.05-LNMO (540 Wh kg^{-1}) and LNMO (527 Wh kg^{-1}). During long-term testing, the Mg0.1-LNMO sample has the highest energy efficiency of ~ 97.5%, and maintains 85.4% of its initial energy density after 1500 cycles, without the rapid energy density decay observed for the Mg0.05-LNMO and LNMO samples. More importantly, the Mg0.1-LNMO manifests an exceptionally high-rate performance, delivering an energy density of around 467 Wh kg^{-1} at 10 C and maintaining 88.2% (412 Wh kg^{-1}) after 1500 cycles, making it a promising candidate material for commercialization.

The rate capabilities of undoped and Mg-doped LNMO were further evaluated with results shown in **Figure 3e**. Unsurprisingly, the Mg0.1-LNMO shows the best rate performance with a specific capacity of up to 111.5 mAh g^{-1} under 5 C, which corresponds to 88.5% of its initial capacity at 0.1 C. However, Mg0.05-LNMO and LNMO, have discharge capacities at 5 C of only 97.1 and 77.5

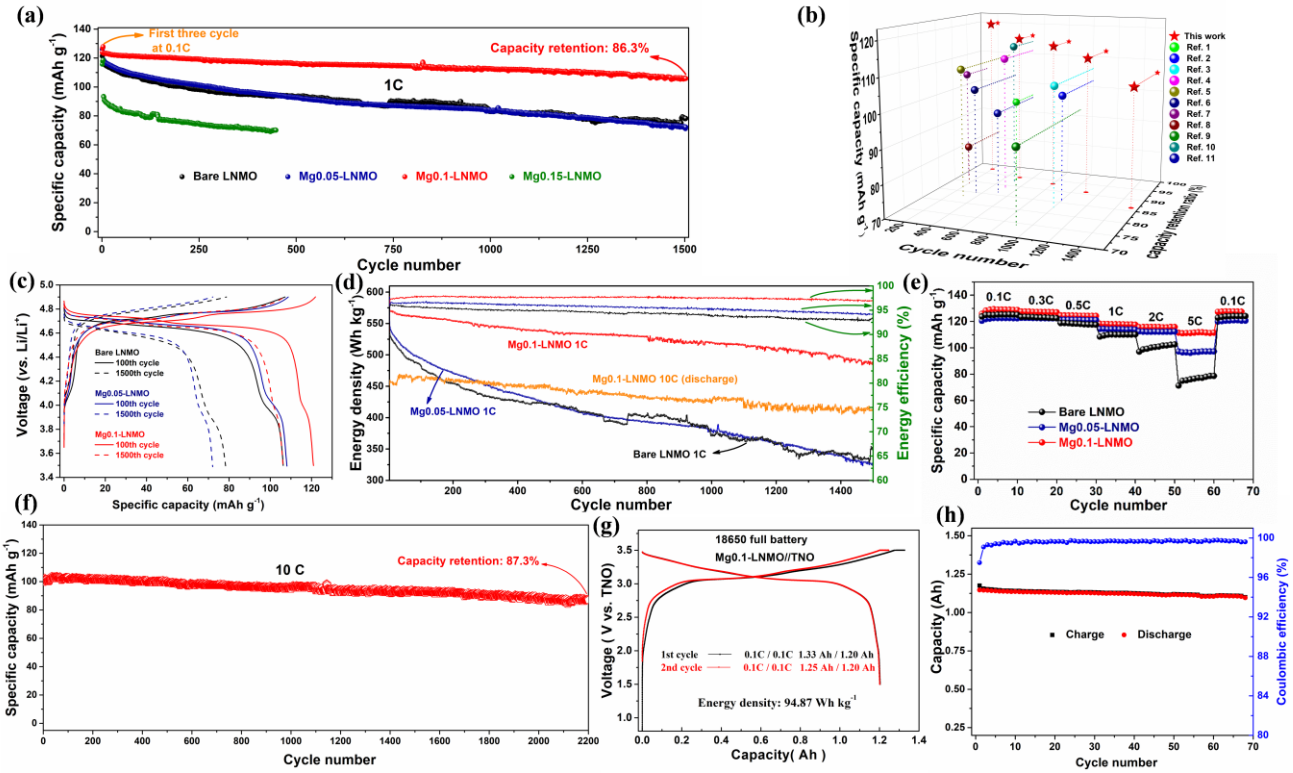

Figure 3. (a) Cycle performance at 1 C of LNMO; (b) cycle stability of Mg0.1-LNMO and other LNMO materials previously reported; (c) charge/discharge curves for the 100th and 1500th cycle of the LNMOs; (d) energy density of LNMO, Mg0.05-LNMO, and Mg0.1-LNMO during cycling with corresponding energy efficiency; (e) rate capability of LNMO, Mg0.05-LNMO, and Mg0.1-LNMO; (f) cycle performance at higher current density (10 C) of Mg0.1-LNMO; (g) charge/discharge curves of a Mg0.1-LNMO//TNO full battery in the first two cycles; (h) cycle performance of the Mg0.1-LNMO//TNO full battery

mAh g^{-1}, respectively, corresponding to 80.9% and 62.6% of their initial capacities at 0.1 C, respectively. The improved rate capability of Mg0.1-LNMO is also verified by CV and electrochemical impedance spectroscopy (EIS) characterization (**Figure S5a** and **S5b**). We note that the two-site doping does not substantially affect the fast diffusion of Li within the spinel structure, as indicated by the similar values of the Li diffusion coefficient for the samples (**Table S4**).

Long-term testing at higher current (**Figure 3f**) shows that Mg0.1-LNMO can deliver a discharge capacity as high as 103.4 mAh g^{-1} at 10 C and maintain 87.3% of the initial discharge capacity after 2200 cycles, corresponding to a capacity decay of only 0.00579% per cycle. The superior cycle performance of the Mg0.1-LNMO sample at both small and large current density further confirms the success of two-site doping. To conclude, Mg doping at both tetrahedral and octahedral sites significantly improves the cycle, energy, and rate performance of LNMO, through effectively mitigating the formation of Mn^{3+} and suppressing Jahn-Teller distortion, and reducing voltage polarization during cycling.

Considering the superior electrochemical performance of Mg0.1-LNMO in half cells, its performance in a full-battery configuration was tested using TNO counter electrode, a promising high-rate replacement for $Li_4Ti_5O_{12}$ (LTO). The crystallography structure, particle morphology, and half-cell performance of TNO are shown in **Figure S6**. **Figure 3g** shows the electrochemical performance of a full battery containing Mg0.1-LNMO and TNO in the first two cycles at 1.5 - 3.5 V. The charge and discharge curves in the first and second cycle overlap well, indicating good cycle stability of the full cell. A flat operating plateau at around 3.0 V for charge and discharge are clearly observed, and minor voltage polarization between charge and discharge is noted due to the desirable kinetics within the full battery. The prototype full battery delivers a discharge capacity of 1.20 Ah in the first two cycles and achieves an energy density of 94.87 Wh kg^{-1} (calculation based on the weight of the whole battery). The cycle performance of the Mg0.1-LNMO//TNO full battery is shown in **Figure 3h**, where the capacity in the 68th cycle still reaches 96.3% of the initial capacity with a columbic efficiency of around 99.7%, indicating its feasibility for large-scale application. In comparison, a LNMO//TNO cell shows inferior battery performance with smaller whole battery capacity and lower columbic efficiency (**Figure S5c** and **S5d**).

In operando and ex situ mechanistic studies

The origin of the outstanding electrochemical performance of the two-site Mg-doped LNMO was explored using in operando synchrotron-based XRPD, where the phase transformation and structural changes of both undoped LNMO and Mg0.1-LNMO during charge/discharge were compared in coin-type half-cells. Disordered LNMO undergoes a solid-solution (one-phase) reaction during the Ni^{2+}/Ni^{3+} redox transformation at approximately 4.6 V (vs. Li/Li^+, from $LiNi_{0.5}Mn_{1.5}O_4$ to $Li_{0.5}Ni_{0.5}Mn_{1.5}O_4$) and a two-phase reaction during the Ni^{3+}/Ni^{4+} redox transformation when the voltage is above 4.7 V (from $Li_{0.5}Ni_{0.5}Mn_{1.5}O_4$ to $Ni_{0.25}Mn_{0.75}O_2$).[19] The two-phase reaction usually occurs through a nucleation and growth mechanism involving grain boundary movement, which negatively impacts the lithiation/delithiation processes.[20] In contrast, the solid-solution reaction is more favorable due to the moderate structural transformation and better cycling reversibility.

Figure 4a and **4b** show in operando synchrotron XRPD data of coin cells containing LNMO and Mg0.1-LNMO, respectively, as a contour plot with intensity in color, along with corresponding electrochemical curves. Three diffraction peaks at approximately 8.3º, 16.0º, and 25.2º correspond to the spinel LNMO 111, 311, and 511 reflections, respectively, with the strongest 111 reflection the focus in the following discussion.

In LNMO, the 111 reflection shifts gradually to higher angles from the open-circuit voltage (OCV) to approximately 4.7 V. During this process, LNMO undergoes a solid-solution reaction as Li ions are extracted from the spinel structure, leading to a decrease of the lattice parameter and cell volume. As the voltage increases, the 111 reflection broadens and experiences intensity changes, before sharpening and shifting to around 8.45º. As the voltage approaches 4.9 V, a weak reflection at around 8.54º arises indicating the formation of $Ni_{0.25}Mn_{0.75}O_2$ rock-salt and a two-phase reaction. We note that the peak intensity of the $Ni_{0.25}Mn_{0.75}O_2$ phase continues to increase at the beginning of discharge, indicating hysteresis in the phase transformation of LNMO, potentially as a result of the relatively-large average particle size (~ 3 μm) of the active material, and a similar phenomenon was reported by Singer *et al*.[21] As the voltage decreases from 4.9 V to approximately 4.66 V, the two reflections coexist, indicating a two-phase reaction. Subsequently, the $Ni_{0.25}Mn_{0.75}O_2$ reflection disappears and the LNMO reflection shifts rapidly to lower angles, corresponding to the process of lithium insertion into the spinel.

In contrast, the Mg0.1-LNMO 111 reflection shifts continuously to higher angles during the whole charge process, with an intensity that varies more moderately than that of the undoped LNMO. During discharge, the Mg0.1-LNMO 111 reflection shifts gradually and reversibly back to a lower angle. Notably, no $Ni_{0.25}Mn_{0.75}O_2$ reflection was found during either charge or discharge, indicating a solid-solution behavior during lithiation/delithiation processes, which ensures the superior structure and cycle stability of Mg0.1-LNMO sample. The absence of the two-phase reaction in the Mg-doped LNMO may be attributed to the elevated difficulty for transition metal to move to neighbor empty octahedral sites and to the disturbance of the cation ordering in the spinel structure with the existence of two-site Mg dopants.

Single-peak fitting of the LNMO 111 reflection was carried out to investigate the structural response and structure-function relation in undoped LNMO (**Figure 4c**) and Mg0.1-LNMO (**Figure 4d**) during cycling. When the voltage is above 3.1 V, the 111 reflection shifts to higher angle as the lattice parameter decreases by 1.11% for the LNMO (0.0913(2) Å, from 8.1956(1) to 8.1043(1) Å) during solid-solution reaction, while Mg0.1-LNMO only experiences a 1.06% decrease in lattice (0.0874(4) Å, from 8.2025(2) to 8.1151(2) Å) although its solid-solution reaction lasts the whole charge process. The smaller structural change of the Mg0.1-LNMO sample during cycling contributes to its superior cycle stability. Ex-situ X-ray absorption spectroscopy (XAS) characterization (**Figure S7**) further confirms the superior structural stability of Mg0.1-LNMO during cycling, with fewer

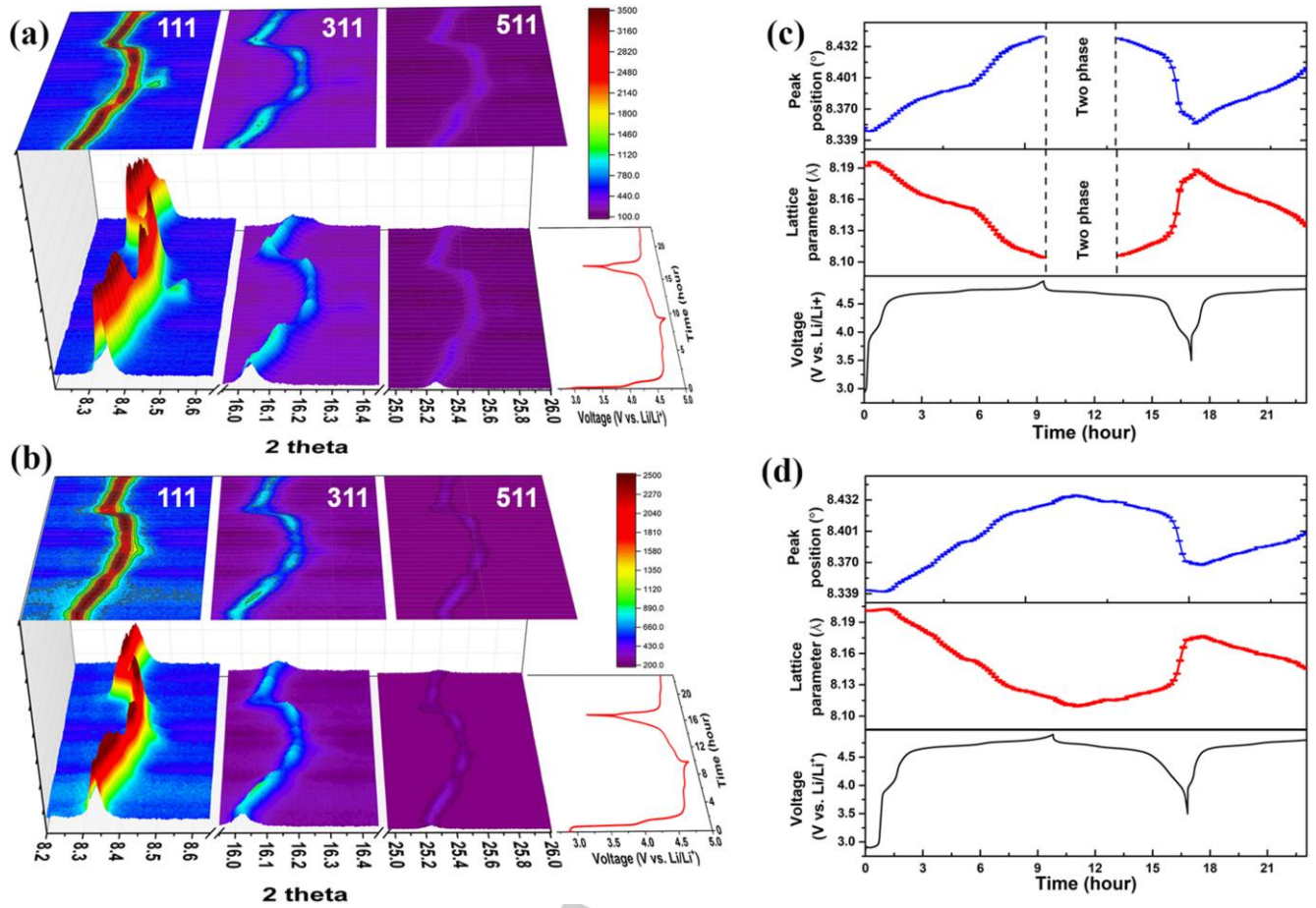

Figure 4. In operando synchrotron XRPD data in a selected 2-theta region shown as a contour plot with intensity in color, the legend for which is shown inset, for (a) LNMO and (b) Mg0.1-LNMO, where the evolution of LNMO 111, 311, and 511 reflections can be seen along with the corresponding charge/discharge curve; single peak fitting results of the 111 reflection of (c) LNMO and (d) Mg0.1-LNMO.

changes in Ni-O and Mn-O bond length relative to the undoped LNMO during charge/discharge. Conclusively, our site-selective Mg doping stabilizes the LNMO structure, and improves cycle stability and electrochemical performance of LNMO due to the less structural change and disappearance of the undesirable two-phase reaction at highly delithiated states.

With its properties of high penetration power and non-destructive interaction, in operando NPD was used to investigate the phase transformation and structural change of both LNMO and Mg0.1-LNMO in 18650-type full cells with TNO as counter electrodes. A further two of these batteries were also examined in their 69th cycle. In operando NPD data for the Mg0.1-LNMO//TNO full battery in the first cycle is presented over the full-angular-range as a contour plot with intensity in color (**Figure 5a**), alongside the corresponding charge and discharge curve. In order to show the structural changes of the LNMO and TNO in detail, contour plots in selected 2θ ranges are shown in **Figure 5b** and **Figure 5c**, respectively. The corresponding NPD data of the bare LNMO//TNO, cycled LNMO//TNO, and cycled Mg0.1-LNMO//TNO in selected 2θ ranges are given in **Figure S8**. The peak at approximately 61.5º corresponds to the LNMO 222 reflection. During cycling, the LNMO 222 reflection shifts to a higher angle during charge and back to the lower angle during discharge. The high structural reversibility and absence of a two-phase reaction observed during this process are consistent with our observations using in operando synchrotron-based XRPD for the half-cell configuration.

The peaks at approximately 38.0º, 78.9º, and 120.5º correspond to the TNO 110, 020, and 025 reflections, respectively. The position of the TNO 110 reflection shifts to a lower angle during charge and back to a higher angle during discharge, as expected from previous work.[22] The TNO 025 reflection position is not linear in its positional evolution during this process, which may be related to the non-monotonic evolution of the TNO *c* lattice parameter during cycling, as previously noted.[22] Overall, our in operando NPD measurements show that both electrodes function well in the prototype full-battery.

Single-peak fitting of the LNMO 222 reflection in the in operando NPD measurements of all full batteries was performed, with results shown in **Figure 5d**, **5e,** and **S8**. The maximum change of the LNMO 222 reflection position between uncycled and various states of charge in the four full batteries are summarized in **Table S5**. After a full charge, the LNMO 222 reflections from both LNMO and Mg0.1-LNMO containing batteries undergo an approximate 1% shift to higher 2θ. After a full cycle, the 222 reflections of undoped and cycled LNMO show a measurable increase, 0.30 and 0.03%, respectively. In the case of Mg0.1-LNMO, however, there is almost no change in the 222 reflection position in the Mg0.1-LNMO//TNO battery, in both fresh and cycled batteries, further verifying its superior structural stability induced by the two-

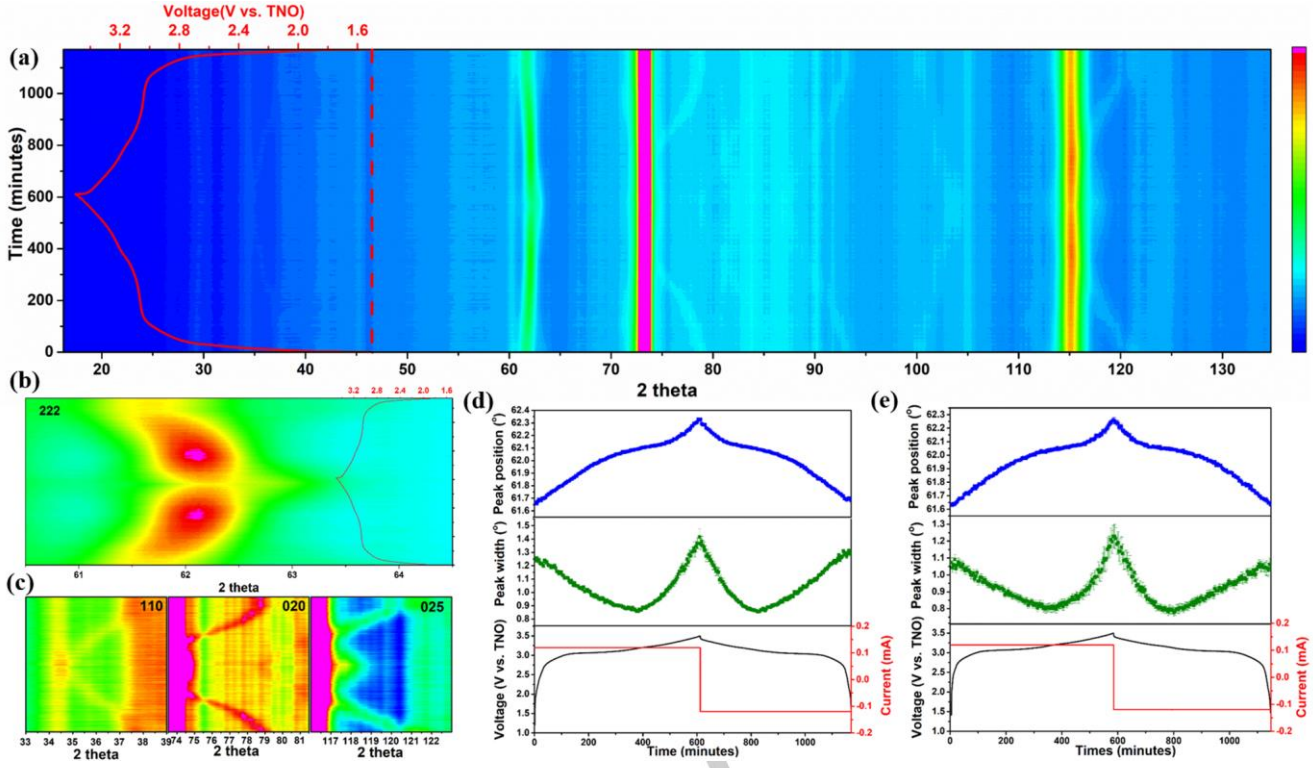

Figure 5. (a) Contour plot of in operando NPD data of Mg0.1-LNMO//TNO full battery at the first cycle; (b) selected 2 theta region showing the changes of LNMO 222 reflection; (c) selected 2 theta regions showing the changes of TNO 110, 020, 025 reflections; single peak fitting results of LNMO 222 reflection evolution in Mg0.1-LNMO//TNO full battery at (d) the first and (e) 69th cycle.

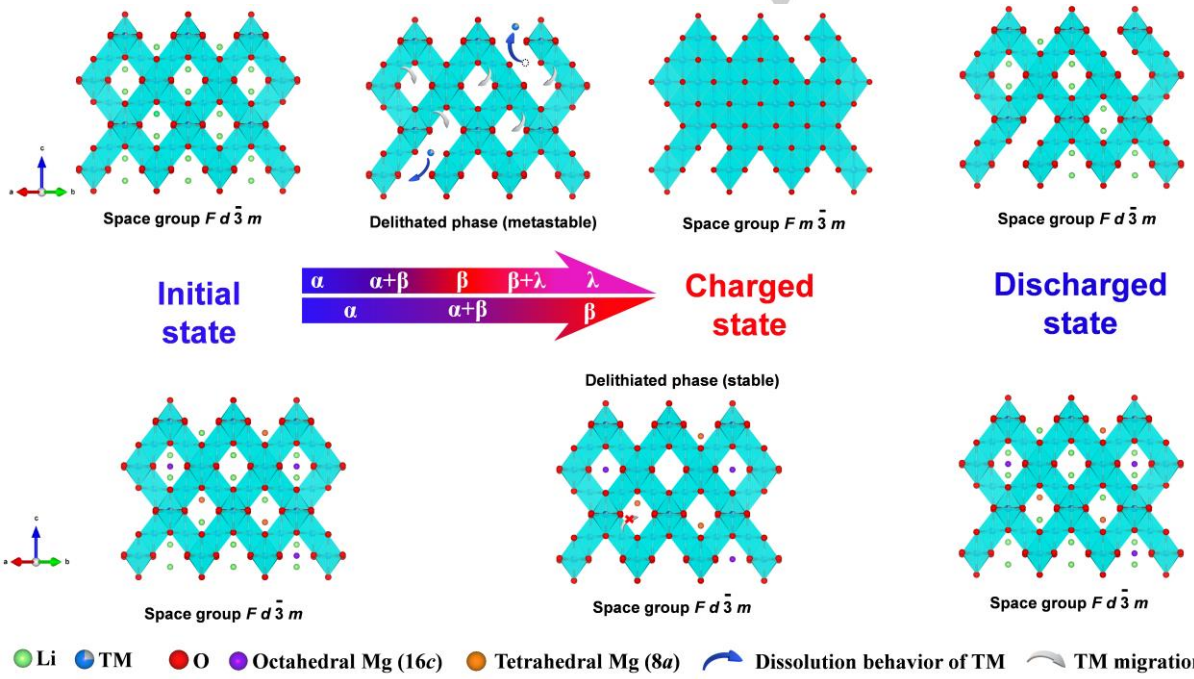

Scheme 1. Schematic illustration of the structural changes and phase evolution of undoped LNMO and Mg0.1-LNMO during charge and discharge, where α, β, λ stand for the uncycled LNMO, delithiated LNMO, and rock-salt phase, respectively. The octahedra containing Ni/Mn are shade in cyan.

site Mg doping. In addition, we also quantify the rate of lithium extraction from LNMO by examining the rate of change of the LNMO 222 reflection position in the 69th cycle, noting a faster delithiation rate for the Mg0.1-LNMO//TNO (0.00630(3) º per min) than the LNMO//TNO (0.00607(1) º per min), corresponding to better Li transport within the Mg-doped LNMO, which is probably due to whole solid-solution reaction process during charging.

In summary, the high cycle stability of the Mg0.1-LNMO material was demonstrated in both half and full-cell configurations. The role of the Mg dopant in achieving this superior stability is

illustrated in **Scheme 1**, where at highly-delithiated state, Mg ions, residing at both 8*a* and 16*c* sites in the *Fd*$\bar{3}$*m* structure, serve as structural pillars, stabilizing the spinel structure, prohibiting the migration of TM ions and thus preventing the formation of a rock-salt type phase. This strategy of doping Mg ions at both 8*a* and 16*c* crystallographic sites in the spinel contributes to the resultant minor structural change and alleviated side reactions of the TM loss during charge/discharge, efficiently resolving the long-standing short-cycle-life issues of LNMO, and could easily be extended to other battery electrode materials.

Conclusion

In conclusion, we successfully employ site-selective Mg doping to stabilize LNMO during electrochemical processes. Notably, the stabilization offered by the Mg doping becomes more prominent at increased cycling, where the optimized Mg-doped LNMO (Mg0.1-LNMO) achieves a capacity retention of 86.3% after 1500 cycles at 1 C and 87.3% after 2200 cycles at 10 C.

We explore in detail the underlying chemistry- and structure-function of Mg-doped LNMO. During cycling, Mg in the Mg0.1-LNMO resides at both 8*a* and 16*c* crystallographic sites in the *Fd*$\bar{3}$*m* structure, mitigating against the dissolution of transition metals, preventing the formation of the undesirable *Fm*$\bar{3}$*m* rock-salt phase and subsequent two-phase reaction, which in turn reduces the Jahn-Teller distortion and voltage polarization. We also demonstrate the effectiveness of the Mg0.1-LNMO electrode material in a full-battery configuration against the novel $TiNb_2O_7$ anodes, further confirming the stabilization brought by Mg dopants.

This work provides a new strategy for the chemical modification of electrode materials that may be applied more generally in battery researches, whereby dopants may be used strategically to address specific electrode issues.

Acknowledgments

This work was supported by the Australian Research Council for FT160100251. The authors thank the Australian Institute of Nuclear Science and Engineering (AINSE) Limited for providing financial assistance in the form of a Post Graduate Research Award (PGRA) to carry out this work. The authors appreciate the operational support of ANSTO staffs for the in operando synchrotron and neutron diffraction experiments. The financial support from the University of Wollongong through the UIC International Links Grant Scheme 2019 (888/006/397) are gratefully acknowledged. In addition, the authors thank the Electron Microscopy Centre (EMC) at the University of Wollongong for the support and equipment assistance. The authors also thank Dr. Tania Silver for critical reading of the manuscript.

Keywords: spinel cathode • high energy density • long cycle life • site-selective doping • chemistry/structure-function

[1] a) B. Dunn, H. Kamath, J.-M. Tarascon, *Science* **2011**, *334*, 928-935; b) J. B. Goodenough, *Acc. Chem. Res.* **2012**, *46*, 1053-1061; c) K. Kang, Y. S. Meng, J. Bréger, C. P. Grey, G. Ceder, *Science* **2006**, *311*, 977-980.

[2] a) J. Y. Piao, L. Gu, Z. Wei, J. Ma, J. Wu, W. Yang, Y. Gong, Y. G. Sun, S. Y. Duan, X. S. Tao, D. S. Bin, A. M. Cao, L. J. Wan, *J. Am. Chem. Soc.* **2019**, *141*, 4900-4907; b) J. Ma, P. Hu, G. Cui, L. Chen, *Chem. Mater.* **2016**, *28*, 3578-3606.

[3] a) T.-F. Yi, J. Mei, Y.-R. Zhu, *J. Power Sources* **2016**, *316*, 85-105; b) A. Manthiram, K. Chemelewski, E.-S. Lee, *Energy Environ. Sci.* **2014**, *7*, 1339.

[4] a) J. Wang, P. Nie, G. Xu, J. Jiang, Y. Wu, R. Fu, H. Dou, X. Zhang, *Adv. Funct. Mater.* **2018**, *28*, 1704808; b) J.-J. Shiu, W. K. Pang, S.-h. Wu, *J. Power Sources* **2013**, *244*, 35-42; c) M.-H. Liu, H.-T. Huang, C.-M. Lin, J.-M. Chen, S.-C. Liao, *Electrochim. Acta* **2014**, *120*, 133-139.

[5] M. Lin, L. Ben, Y. Sun, H. Wang, Z. Yang, L. Gu, X. Yu, X.-Q. Yang, H. Zhao, R. Yu, M. Armand, X. Huang, *Chem. Mater.* **2014**, *27*, 292-303.

[6] B. Xiao, H. Liu, J. Liu, Q. Sun, B. Wang, K. Kaliyappan, Y. Zhao, M. N. Banis, Y. Liu, R. Li, T. K. Sham, G. A. Botton, M. Cai, X. Sun, *Adv. Mater.* **2017**, *29*.

[7] J.-Y. Piao, Y.-G. Sun, S.-Y. Duan, A.-M. Cao, X.-L. Wang, R.-J. Xiao, X.-Q. Yu, Y. Gong, L. Gu, Y. Li, Z.-J. Liu, Z.-Q. Peng, R.-M. Qiao, W.-L. Yang, X.-Q. Yang, J. B. Goodenough, L.-J. Wan, *Chem* **2018**, *4*, 1685-1695.

[8] R. D. Shannon, *Acta Cryst.* **1976**, *32*, 751-767.

[9] a) U. Lafont, C. Locati, W. J. H. Borghols, A. Łasińska, J. Dygas, A. V. Chadwick, E. M. Kelder, *J. Power Sources* **2009**, *189*, 179-184; b) F. Ooms, E. Kelder, J. Schoonman, M. Wagemaker, F. Mulder, *Solid State Ionics* **2002**, *152*, 143-153; c) R. Alcantara, M. Jaraba, P. Lavela, J. Tirado, E. Zhecheva, R. Stoyanova, *Chem. Mater.* **2004**, *16*, 1573-1579; d) C. Locati, U. Lafont, L. Simonin, F. Ooms, E. M. Kelder, *J. Power Sources* **2007**, *174*, 847-851; e) M. Wagemaker, F. G. Ooms, E. M. Kelder, J. Schoonman, F. M. Mulder, *J. Am. Chem. Soc.* **2004**, *126*, 13526-13533.

[10] D. Buchholz, C. Vaalma, L. G. Chagas, S. Passerini, *J. Power Sources* **2015**, *282*, 581-585.

[11] a) H. Liu, R. Kloepsch, J. Wang, M. Winter, J. Li, *J. Power Sources* **2015**, *300*, 430-437; b) H. Liu, J. Wang, X. Zhang, D. Zhou, X. Qi, B. Qiu, J. Fang, R. Kloepsch, G. Schumacher, Z. Liu, J. Li, *ACS Appl. Mater. Interfaces* **2016**, *8*, 4661-4675.

[12] a) Y. Liu, Z. Lu, C. Deng, W. Xu, T. Hu, B. Yan, G. Yang, *ChemElectroChem* **2017**, *4*, 1205-1213; b) B. Xiao, J. Liu, Q. Sun, B. Wang, M. N. Banis, D. Zhao, Z. Wang, R. Li, X. Cui, T. K. Sham, X. Sun, *Adv. Sci.* **2015**, *2*, 1500022.

[13] B. Zheng, S. Wu, X. Yang, M. Jia, W. Zhang, G. Liu, *ACS Appl. Mater. Interfaces* **2016**, *8*, 26683-26689.

[14] C. H. Van Oversteeg, H. Q. Doan, F. M. de Groot, T. Cuk, *Chem. Soc. Rev.* **2017**, *46*, 102-125.

[15] W. Bronger, H. Bade, W. Klemm, *Z. Anorg. Allg. Chem.* **1964**, *333*, 188-200.

[16] H. Berg, J. O. Thomas, W. Liu, G. C. Farrington, *Solid State Ionics* **1998**, *112*, 165-168.

[17] W. Liu, Q. Shi, Q. Qu, T. Gao, G. Zhu, J. Shao, H. Zheng, *J. Mater. Chem. A* **2017**, *5*, 145-154.

[18] a) J. Wang, P. Nie, J. Jiang, Y. Wu, R. Fu, G. Xu, Y. Zhang, H. Dou, X. Zhang, *ChemElectroChem* **2018**, *5*, 1212-1218; b) J.-C. Fang, Y.-F. Xu, G.-L. Xu, S.-Y. Shen, J.-T. Li, L. Huang, S.-G. Sun, *J. Power Sources* **2016**, *304*, 15-23; c) H. B. Lin, Y. M. Zhang, J. N. Hu, Y. T. Wang, L. D. Xing, M. Q. Xu, X. P. Li, W. S. Li, *J. Power Sources* **2014**, *257*, 37-44; d) X. Fang, N. Ding, X. Y. Feng, Y. Lu, C. H. Chen, *Electrochim. Acta* **2009**, *54*, 7471-7475; e) J. M. Lim, R. G. Oh, D. Kim, W. Cho, K. Cho, M. Cho, M. S. Park, *ChemSusChem* **2016**, *9*, 2967-2973; f) J. Chong, S. Xun, X. Song, G. Liu, V. S. Battaglia, *Nano Energy* **2013**, *2*, 283-293; g) Y. Xue, Z.-B. Wang, L.-L. Zheng, F.-D. Yu, B.-S. Liu, Y.-X. Zhou, *ChemistrySelect* **2017**, *2*, 4325-4331; h) D. Lu, L. Yuan, Z. Chen, R. Zeng, Y. Cai, *J. Alloys Compd.* **2018**, *730*, 509-515.

[19] a) W. K. Pang, N. Sharma, V. K. Peterson, J.-J. Shiu, S.-h. Wu, *J. Power Sources* **2014**, *246*, 464-472; b) H. Liu, G. Liang, C. Gao, S. Bi, Q. Chen, Y. Xie, S. Fan, L. Cao, W. K. Pang, Z. Guo, *Nano Energy* **2019**, *66*, 104100.

[20] V. K. Peterson, J. E. Auckett, W. K. Pang, *IUCrJ* **2017**, *4*, 540-554.
[21] A. Singer, A. Ulvestad, H. M. Cho, J. W. Kim, J. Maser, R. Harder, Y. S. Meng, O. G. Shpyrko, *Nano Lett.* **2014**, *14*, 5295-5300.
[22] H. Yu, H. Lan, L. Yan, S. Qian, X. Cheng, H. Zhu, N. Long, M. Shui, J. Shu, *Nano Energy* **2017**, *38*, 109-117.

Table of Contents

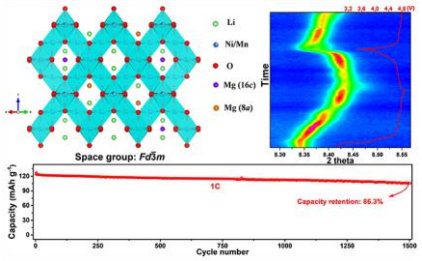

Gemeng Liang, Zhibin Wu, Christophe Didier, Wenchao Zhang, Jing Cuan, Baohua Li, Kuan-Yu Ko, Po-Yang Hung, Cheng-Zhang Lu, Yuanzhen Chen, Grzegorz Leniec, Sławomir Maksymilian Kaczmarek, Bernt Johannessen, Lars Thomsen, Vanessa K. Peterson, Wei Kong Pang*, Zaiping Guo*

A long cycle-life high-voltage spinel lithium-ion battery electrode achieved by site-selective doping

Mg, which is selectively doped onto both tetrahedral (8*a*) and octahedral (16*c*) sites in the *Fd*$\bar{3}$*m* $LiNi_{0.5}Mn_{1.5}O_4$, could stabilize the structure against structural deformation and suppress the unfavorable two-phase reactions during cycling process, thus contributing to an excellent extended-long-term electrochemical performance.